Friedrich Schiller Universität Jena
PAF

Dissertation

High-Fluence Ion Beam Irradiation of Semiconductor Nanowires

Andreas Johannes

März 2015

Abstract

Hier alles Bla

Contents

1 Introduction

2 Background

To put the experimental details and results into a more general scientific context it will be useful to provide some background. First a general outline of energetic ion-solid interaction is given. Then the possibilities of simulating this ion-solid interaction are discussed with an emphasis on those effects that will be relevant to the experiment in this thesis.

2.1 Ion-solid interaction

Energy loss

An energetic ion impinging on a solid will lose its kinetic energy to the solid in a variety of processes. The stopping power is well described for a large energy range by the Bethe (sometimes "Bethe-Bloch") formula derived using the Born approximation perturbation theory on the impact between the 'fast' ion and the 'slow' electrons in the solid:

$$S = \frac{dE}{dx} = -A \cdot \frac{\rho\, Z_2 \cdot Z_1^2}{\beta^2} \cdot \left[ln\Big(\frac{B \cdot \beta^2}{Z_2 \cdot (1-\beta^2)} \Big) - \beta^2 \right], \tag{2.1}$$

with A and B positive combinations of constants, ρ the density and Z_2 the atomic number of the target, Z_1 and $\beta = v/c$ the atomic number and relativistic velocity of the ion. Corrections to this formula are especially necessary for low ion energies, but in detail they are dependent on the

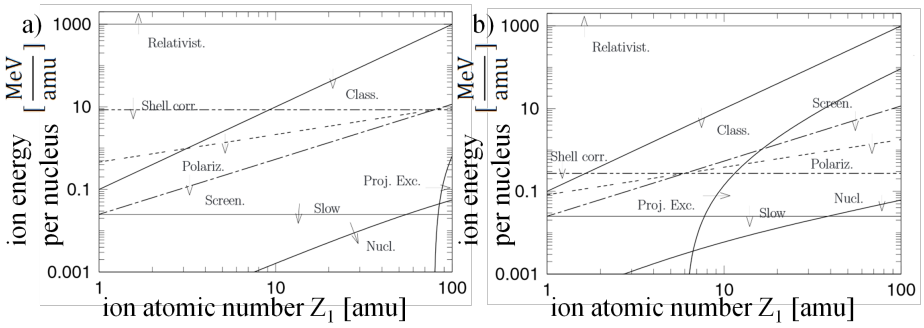

Figure 2.1: Illustration of the dominant effects on the stopping power for an ion of mass Z_1 and energy E in Au a) and C b). Adapted from [Sig04].

target composition, the ion energy and ion mass in a non-trivial way. Figure 2.1 and following discussion illustrates stopping regimes and why corrections are required to the Bethe formula. It is adapted from [Sig04].

At high ion energies ($> 1\,GeV/amu$, labeled "Relativist.") highly relativistic effects have to be taken into account. At these energies we have, for example, Cherenkov radiation. Nuclear reactions and resonances may play a role at lower energies already, especially for light ion-target combinations. As nuclear reactions may change the ion species, their cross sections are typically treated separately from the stopping power.

The horizontal line labeled "Shell corr." marks the Thomas-Fermi velocity ($Z_2^{2/3} v_0$) of the target electrons. The constant $v_0 = e^2/\hbar = 25\,keV/amu$ is the Bohr velocity. In the parameter-space below this line the ion is moving at speeds comparable to that of the electrons in the target. In the low energy area below the line labeled "Slow" ($25\,keV/amu$) the ion is traveling at speeds below the Bohr velocity of the target electrons. Here the ion velocity is only comparable to that of the valence electrons in the solid. Both these points mean that the actual electron density distribution and chemical nature of the solid becomes relevant, which is of course not considered in the general Bethe formula.

Above the line showing the Thomas-Fermi velocity of the ion ($v = Z_1^{2/3} v_0$, "Screen.") the ion can be assumed to be stripped of all its electrons. Below, a screening function must consider the effective charge of the ion. Below the curve labeled "Proj. Ext." the ion (projectile) carries a comparable number of electrons to the target making excitation processes in the electronic configuration of the ion significant.

For ion velocities $v < (Z_1 Z_2)^{1/3} v_0$ (labeled "Polariz.") a higher order (Z_1^3) correction term to the Bethe formula becomes relevant due to the Barkas-Andersen effect. Below the line marked "Class." ($Z_1^2 \cdot 100\, keV/amu$) classical Bohr orbits can be used for electrons around the ion, this is a *sufficient* criterion for the derivation of the Bethe formula not a *necessary* one.

Finally, not be confused with the nuclear reactions already mentioned, in the region marked "Nucl.", for low energies and large ions, interaction with the electronic system become low. Here the contribution of the coulomb interaction between ion and individual target atoms as a whole become the main contribution to slowing the ion. This is called nuclear stopping in contrast to the electronic stopping discussed so far as kinetic energy is transferred to the whole atom, which can be treated as nucleus with an interaction potential with the ion.

The effects that the ion-solid interaction has on the solid can be discussed well by looking at the electronic and nuclear energy loss separately.

Effects of electronic energy loss

"Exciting the electronic system" is a somewhat general expression referring to a large array of effects. Ionization of target atoms is followed by a host of effects such as characteristic X-ray emission, Auger electron emission,

Effects of nuclear energy loss

The most straightforward process in the energetic ion-solid interaction is an elastic collision between the impinging ion and a target atom.

interaction potentials [Ded95]

2.2 Simulation of ion-solid interaction

Melecular dynamic simulations

MD general: cite Alder, Nordlund+Kuronen MD interatomic potentials: Runeberg+Sundholm, Nordlund+Dudarev, properties of GaAs: Albe+Nord+Nordlund

Monte-Carlo and the binary collision approximation

BCA, MC Ausgiebige Verwendung von *iradina* [BR11]

3 Experimental Methods

The respective machines, technologies and concepts used within this dissertation can not be fully characterized within a couple of pages. This section will mainly serve as a glossary of the methods, abbreviations and acronyms used in the following dissertation which not every reader may be familiar with. Further, only an incomplete collection of references to textbooks and literature can be given.

3.1 Nanowire synthesis

Nanostructures can generally be synthesis can be categorized according to two approaches: "bottom-up" and "top-down". The "bottom-up" approach relies on the self-organized arrangement of matter using an inherent anisotropy in one of the thermodynamic properties of the relevant system to create nanoscale structures. Depending on the material, crystal quality, morphology, infrastructure requirements, the quantity to be produced etc. there is a large variety of processes available for synthesis. For semiconductor nanowires the main approaches developed are based on hydro-thermal, pyrolytic, vapor-transport, chemical vapor deposition, laser ablation, metal organic vapor phase epitaxy (MOVPE), molecular beam epitaxy (MBE) processes, in ascending order of complexity, or number of controllable parameters.

A very common mechanism to create the anisotropy required to get the one dimensional growth required to obtain nanowires is the vapor-liquid-solid growth (VLS) first described by Wagner and Ellis. The variety of processes listed before are responsible to provide the 'vapor' of material for this growth mechanism. With vapor transport the source material eg. ZnO is simply evaporated in a typically inert atmosphere and transported within an oven to the substrate by diffusion or gas flow. Chemical vapor deposition uses reactive gases such as SiH_3 to provide the material, in this case Si in a temperature and pressure controlled oven. Similarly in MOVPE a metal-organic gas is used as at least one of the sources. For example TMG (trimethylgallium) and AsH_3 to grow $GaAs$.

Although also self-catalyzed growth has been observed, the liquid part in VLS is typically played by a metal catalyst deposited on the growth substrate. The material in the vapor phase can collect in the catalyst droplet until the concentration is saturated. Preferential segregation of the nanowire material at the droplet-substrate interface leads to the growth of a wire. The size of the droplet can be used to control the diameter of the grown nanowire to some extent. ZnO [BMS+06, Sti08, Mü09, Ogr13], $GaAs$ [BDSS04, WDJ+09] and Si [LSH+08] nanowires investigated in this dissertation where grown with the VLS mechanism using vapor transport, MOVPE and chemical vapor deposition respectively. An epitaxial relation between the substrate and the nanowire material may be used to direct the growth. Typical nanowire diameters and lengths are $50 - 300\,nm$ and $> 10\,\mu m$ respectively.

Nanowires can also be synthesized "top-down". A "top-down" approach requires a predefined template which is used to control the desired morphology. The Si-nanowire arrays investigated within this dissertation were etched by reactive ion etching (RIE) through a circular Ni hard-mask which defined the nanowire diameter *cite NL* . The

"top-down" etching process was used, as with it it is possible to prepare nanowires with diameters varying from $50\,nm$ to $2\,\mu m$ with a height of $\approx 3\mu m$ on a single substrate.

Since the growth itself was performed mainly by collaborators in Lund University ($GaAs$) and TU Vienna (Si) and is not part of the investigations reported here, the inclined reader is redirected to the the cited references for further details respective growth parameters and their investigation.

3.2 Modification

ROMEO

The ion irradiation for this dissertation was performed at the general purpose HVE implanter "ROMEO" at the IFK in Jena. It can provide an ion beam of virtually any element at energies of $10 - 380\,keV$. The beam passes a 90° selector magnet and can be sweeped with a frequency of kHz to homogeneously irradiate areas up to several tens of cm^2 with ion currents of up to $1\,mA$. For this work ion current densities were limited to $500\,nA/cm^2$ or $10^{16}\,ions/cm^2$ in $15\,min$. As previous work has shown that the irradiation of nanowires can bend the nanowires [BSL$^+$11, Bor12], a rotatable and heatable, tilted stage (RHT) was custom built [Noa14]. With it bending of the nanowires grown upstanding on a substrate can be avoided as they are irradiated homogeneously from all sides at an angle of 45°. All the samples investigated in this thesis were rotated on the RHT and its preceding prototype sample stages during the irradiation.

FIB

Some sample preparation required a focused-ion-beam (FIB). FIBs are highly specialized ion accelerators where the main objective is to obtain a small ion beam focus. The most wide spread systems use a Ga^+ beam and acceleration voltages up to $30\,keV$. The main use for FIBs is to use the focused ion beam to sputter material extremely locally, making it a versatile tool for nano-machining. The FEI DualBeam Helios NanoLab 600i FIB system used for this dissertation is a scanning electron microscope (SEM) - FIB combination, so that the sample can be milled with the ion beam and investigated with the SEM. It also is equipped with a Pt-metal-organic-gas injection system. The Pt containing organic gas can be cracked locally on the sample by the secondary electrons created by either the electron or the ion beam. Most of the Pt is deposited near the impact point of the primary beam and the substrate, however typically a rather large 'halo' of minor Pt deposition can extend for a couple of μm. The FIB system can thus deposit and mill structures on a nm scale.

3.3 Characterization

SEM

The morphological changes in the nanowires were characterized by high resolution SEM in the FEI DualBeam Helios NanoLab 600i focused-ion beam system. The spacial resolution of the SEM system is $\approx 2\,nm$. To quantify the sputtering images of individual nanowires were made before and after ion irradiation. To find exactly the same place on the sample, a series of images with increasing magnification has to be made. Typically images were made at an angle of 45° to the substrate with the substrate aligned the same way before and after irradiation.

An semi-automated image analysis protocol was developed by Stefan Noack in his Master thesis [Noa14, **?**] to evaluate the SEM images of a large number of nanowires. It applies a (3x3) median filter to smoothed out some noise and a Gaussian unsharp mask with $\sigma = 1\,px$ and weighted at 60 % to resharpened the edges [San04]. An Otsu thareshold [Ots79] is applied to separate the lighter nanowire from the darker background. Next, open source particle analysis software is used to find the main body of the nanowire and turn the it upright, correcting for any marginal tilt remaining in the SEM images [SACF$^+$12, SPTS12]. Finally the sum of the gray-values in each line used to calculate the diameter at that height along the nanowire axis. As the investigated nanowires showed a characteristic bulge at the base, this point can be used to align the height profiles of a single wire before and after irradiation.

EBSD

Electron back-scatter diffraction (EBSD) was used to identify whether nanowires remained crystalline after irradiation with a Carl Zeiss Auriga CrossBeam Workstation. EBSD can be measured with a large CCD detector in a SEM. The electron beam is focused on the sample at an arbitrary angle. Electrons are scattered from the sample lattice and the scattered electrons are detected by the CCD detector. Bragg diffraction along the crystal lattice planes produces a characteristic pattern of Kikuchi lines on the detector [Kik28, FH13] in crystalline samples. Amorphous or nano-crystalline samples show no pattern.

nano-XRF

The most experimentally advanced characterization method was X-ray fluorescence with a nano-focussed X-ray beam (nano-XRF) at the European Synchrotron Radiation Facility (ERSF), beamlines ID16b and

ID13. Hard X-ray radiation will excite the atoms within a radiated material to emit characteristic X-ray radiation. This X-ray fluorescence can be detected in an energy dispersive semiconductor detector and used to identify and quantify the elements in the sample. In principle the method is similar to the more wide-spread energy dispersive X-ray spectroscopy (EDX), where the electron beam is used to excite characteristic X-ray fluorescence. Very good lateral resolution can be obtained by having an EDX detector in an SEM. The advantage of using X-rays lies in the absence of this Bremsstralung which high energy electrons in matter produce in addition to the characteristic X-rays. In XRF there is thus a much lower background and a much lower concentrations of elements can still be detected and quantified. Unlike normal characteristic X-ray tubes, synchrotron radiation is typically very brilliant, allowing it to be focused. The beamlines ID16b and ID13 were run at various energies above $16\,keV$ and a focus of typically $\approx 80\,nm$ and $\approx 250\,nm$ respectively. The nano-XRF thus allows for quantification of low concentrations with sufficient lateral resolution to resolve axial concentration gradients in a nanowire. Unfortunately, the resolution is not good enough to investigate radial distributions.

At both beamlines the nanowires are scanned under the fixed focal point of the X-ray beam with piezo-motors while the XRF spectra are collected with a Vortex EM silicon drift X-ray detector. The investigated Mn irradiated ZnO nanowires were deposited on TEM grids either randomly by 'imprinting' or individually by using the mico-manipulator in the FEI DualBeam FIB. Transferring individual wires requires some finesse, but it is possible to detach the ZnO nanowires from their substrate without the Ga FIB and to place them on the "lacey-carbon" TEM Grids without any additional Pt deposition. In this way SEM images before and after irradiation of the same wire investigated by nano-XRF are available.

The spectra used for quantification were obtained in multiple scans across a nanowire at regular intervalls along the nanowire's length. As the XRF signal can be used to locate the nanowire, only the points near the nanowire were measured with a high integration time and a low step-with ($< \frac{1}{2}$ focal spot) to ensure a large number of counts ($> 10^5$ per scan) at reasonable measuring times.

nano-XRF quantification

Spectra were evaluated using the open source PyMCA software package [SPC+07]. The effects of self absorption and excitation can be neglected, as the investigated nanowires are very thin compared to the absorption length of a couple of μm of hard X-rays. However, the detector-sample distance is an unavoidable attenuation length in air, with its absorption by the heaviest element in air, Ar. As the element investigated, Mn, is relatively light, its characteristic X-ray emission at $K_{\alpha,Mn} = 5.9\,keV$ suffers more absorption than the heavier Zn with $K_{\alpha,Zn} = 8.6\,keV$. Thus absorption of the XRF signal in air has to be considered carefully in the fitting with PyMCA. The accuracy was double checked by measuring and quantifying trace elements in a calibration sample of bovine liver. In this way optimal fitting parameters were found and applied to all measured spectra in the PyMCA batch mode. Oxygen can not be quantified in these beamlines, as the signal is attenuated too far. The quantification of the Mn content in the ZnO nanowires thus relies on the assessment of the Mn/Zn ratio. It a decent approximation to assume that the ZnO remains stoichiometric even during the irradiation. The samples are irradiated in a chamber with a base pressure $\approx 10^{-6}\,mbar$, so according to the Hertz-Knudsen equation this will give a coverage of roughly one mono-layer or $10^{15}\,particles/cm^2s$. The maximum ion current density of $500\,nA/cm^2s$ amounts to $10^{13}\,ions/cm^2s$, so that an unlikely amount of

preferential sputtering would be required to deplete the oxygen out of the wires. In any case, the wires will be oxidized in the normal atmosphere post irradiation. The Mn/Zn ratio is thus a good proxy for the Mn concentration.

The quantification limit can be tested within PyMCA by finding an appropriate photon flux and nanowire interaction volume for a simulation to reproduce the XRF spectrum with the actually measured number of counts at $K_{\alpha,Zn}$. The Mn content in the simulated matrix can then be decreased until the minimum Mn content is found which gives a signal at $K_{\alpha,Mn}$ just above the actually measured noise level. In this way a lower limit for the concentration resolution can be found at typically $0.1\,\%Mn/Zn$.

check: Master Thesis Noack, Ogrisek, Conference proceding D. Sage

Bibliography

[BDSS04] M. Borgström, K. Deppert, L. Samuelson, and W. Seifert. Size- and shape-controlled GaAs nano-whiskers grown by MOVPE: a growth study. *Journal of Crystal Growth*, 260(1–2):18–22, January 2004.

[BMS+06] C. Borchers, S. Müller, D. Stichtenoth, D. Schwen, and C. Ronning. Catalyst Nanostructure Interaction in the Growth of 1d ZnO Nanostructures. *The Journal of Physical Chemistry B*, 110(4):1656–1660, February 2006.

[Bor12] Christian Borschel. *Ion-Solid Interaction in Semiconductor Nanowires*. PhD thesis, University Jena, Jena, 2012.

[BR11] C. Borschel and C. Ronning. Ion beam irradiation of nanostructures – A 3d Monte Carlo simulation code. *Nuclear Instruments and Methods in Physics Research Section B: Beam Interactions with Materials and Atoms*, 269(19):2133–2138, October 2011.

[BSL+11] Christian Borschel, Susann Spindler, Damiana Lerose, Arne Bochmann, Silke H. Christiansen, Sandor Nietzsche, Michael Oertel, and Carsten Ronning. Permanent bending and alignment of ZnO nanowires. *Nanotechnology*, 22(18):185307, May 2011. WOS:000288653300010.

[Ded95] Gv Dedkov. The Interatomic Interaction Potentials in Radiation Physics. *Physica Status Solidi a-Applications and Materials Science*, 149(2):453–513, June 1995. WOS:A1995RH61400001.

[FH13] Brent Fultz and James Howe. *Transmission Electron Microscopy and Diffractometry of Materials*. Graduate Texts in Physics. Springer Berlin Heidelberg, Berlin, Heidelberg, 2013.

[Kik28] Seishi Kikuchi. Diffraction of Cathode Rays by Mica. *Proceedings of the Imperial Academy*, 4(6):271–274, 1928.

[LSH+08] A. Lugstein, M. Steinmair, Y. J. Hyun, G. Hauer, P. Pongratz, and E. Bertagnolli. Pressure-induced orientation control of the growth of epitaxial silicon nanowires. *Nano Letters*, 8(8):2310–2314, August 2008. WOS:000258440700034.

[Mü09] Sven Müller. *Structural and optical impact of transition metal implantation into zinc oxide single crystals and nanowires*. PhD thesis, Georg-August Universität Göttingen, Göttingen, 2009.

[Noa14] Stefan Noack. *Sputter Effects of Silicon Nanowires under Ion Bombardment*. University Jena, Master Thesis, 2014.

[Ogr13] Matthias Ogrisek. *Kontrolliertes Wachstum von Zinkoxid und Vanadium(IV)-oxid Nanodrähten*. University Jena, Master Thesis, 2013.

[Ots79] NOBUYUKI Otsu. A Threshold Selection Method from Gray-Level Histograms. *IEEE Transactions on Systems, Man, and Cybernetics*, 9(1):62–66, 1979.

[SACF+12] Johannes Schindelin, Ignacio Arganda-Carreras, Erwin Frise, Verena Kaynig, Mark Longair, Tobias Pietzsch, Stephan Preibisch, Curtis Rueden, Stephan Saalfeld, Benjamin Schmid, Jean-Yves Tinevez, Daniel James White, Volker Hartenstein, Kevin Eliceiri, Pavel Tomancak, and Albert Cardona. Fiji: an open-source platform for biological-image analysis. *Nature Methods*, 9(7):676–682, June 2012.

[San04] B Sankur. Survey over image thresholding techniques and quantitative performance evaluation. *Journal of Electronic Imaging*, 13(1):146, January 2004.

[Sig04] Peter Sigmund, editor. *Stopping of Heavy Ions*, volume 204 of *Springer Tracts in Modern Physics*. Springer Berlin Heidelberg, Berlin, Heidelberg, 2004.

[SPC+07] V. A. Solé, E. Papillon, M. Cotte, Ph. Walter, and J. Susini. A multiplatform code for the analysis of energy-dispersive X-ray fluorescence spectra. *Spectrochimica Acta Part B: Atomic Spectroscopy*, 62(1):63–68, January 2007.

[SPTS12] Daniel Sage, D. Prodanov, J.-Y. Tinevez, and J. Schindelin. ImageJ User & Developer Conference (IUDC'12). 2012.

[Sti08] Daniel Stichtenoth. *Dimensionseffekte in Halbleiternanodrähten*. PhD thesis, Georg-August Universität Götingen, Göttingen, 2008.

[WDJ+09] Brent A. Wacaser, Kimberly A. Dick, Jonas Johansson, Magnus T. Borgström, Knut Deppert, and Lars Samuelson. Preferential Interface Nucleation: An Expansion of the VLS Growth Mechanism for Nanowires. *Advanced Materials*, 21(2):153–165, January 2009.